HiSST: 2nd International Conference on High-Speed Vehicle Science Technology
11–15 September 2022, Bruges, Belgium

Boundary Layer and Transition Onset Assessment on Generic Geometries

J. Paul Hoffmann[1], Jeroen Van den Eynde[2] and Johan Steelant[3]

Abstract

Today's CDF simulations tools and the related computational resources provide the engineers an enormously high-fidelity design tool to generate in a short time span an enormous aerodynamic and aerothermal database, both for the laminar and turbulent state. However, transitional flow simulation is still in its infancy that one still needs to rely on practical engineering correlations composed of typical boundary layer parameters. This work describes the methodology to extract the necessary boundary layer parameters from any vast dataset in an automatic fashion, allowing to apply best-practice correlations on any type of three-dimensional geometrical body. The validation on simple test cases and application on real geometries demonstrates the potential of this engineering methodology.

Keywords: *transition, boundary layer, post-processing*

Nomenclature

Latin
AoA – Angle of attack
C – Correlation constant, Chapman-Rubensin parameter
c – Speed of sound
d – Cavity depth
H_{12} – First shape factor
H_{32} – Second shape factor
$\mathcal{I}_{JST}$ – JST-indicator
k – Roughness element height
Ma – Mach number
p – Pressure
R – Specific gas constant
Re – Reynolds number
Re_{kk} – Roughness Reynolds number
Re_u – Unit Reynolds number
Re_x – Local Reynolds number
Re_θ – Momentum thickness Reynolds number
S – Local streamline length
T – Temperature
t – Time
U – Velocity
u, v, w – Velocity components
x, y, z – Spatial coordinates

Greek
δ – Boundary layer thickness
δ^1 – Displacement thickness
δ^2, θ – Momentum thickness
δ^3 – Energy thickness
γ – Ratio of specific heats, intermittency
Λ – Wing sweep angle
μ – Dynamic viscosity
ϑ – Aileron deflection
ρ – Density
Superscripts
$'$ – Local wall normal coordinate system
$''$ – Local wall normal coordinate system with edge-velocity orientated wall-parallel axis
Subscripts
∞ – Freestream value
aw – Value for the adiabatic wall
e – Value at the boundary layer edge
i – Point index
k – Value at the height of the roughness
s – Sutherland law reference values/constant
t – Transition onset
tr – Transitional
w – Value at the wall

[1] *past: Aerospace engineering student, University of Stuttgart, 70174 Stuttgart, Germany current: PhD Student, German Aerospace Center (DLR) – Institute of Aerodymanics and Flow Technology, Bunsenstraße 10, 37073 Göttingen, Germany, paul.hoffmann@dlr.de*
[2] *Aerothermodynamics Engineer, ESA/ESTEC, 2200AG Noordwijk, The Netherlands, Jeroen.Van.den.Eynde@esa.int*
[3] *Senior Aerothermodynamicist, ESA/ESTEC, 2200AG Noordwijk, The Netherlands, Johan.Steelant@esa.int*

Introduction

Even though the laminar-turbulent transition process is of great importance in many fields of engineering, it is still not completely understood yet nor does a universal transition model exist for CFD tools. Especially in the context of hypersonics, the transition process is directly linked to drastically increased viscous drag and heat loads. The knowledge of the transition onset and its extent for a given flight vehicle is therefore of great value since it would allow an improved design, for example a lower thrust installation and a reduced thermal protection system (TPS) resulting into a lower weight. This observation is further supported by the Defense Science Board which evaluated the U.S. National Aerospace Plane Program (NASP) in 1988 [1]: "Estimates [of transition] range from 20% to 80% along the body …The estimate made for the point of transition can affect the design vehicle gross take-off weight by a factor of two or more". Furthermore, the same National Aerospace Plane review board concluded in 1992 [2]: 'The two most critical [technology areas] are scramjet engine performance and boundary layer transition… Further design development and increased confidence in these two technical areas must be of paramount importance to the NASP program.'

The model-based prediction of transition by means of laminar and/or Reynolds-averaged Navier-Stokes (RANS) simulations is still a research subject. A rather simple method is to enable the turbulence model at a given position. Lacking an actual physical mechanism, this however results in incorrect transition point and length. By using the concept of intermittency, i.e. blending the laminar and turbulent solutions, a more physical and more accurate prediction of the transitional flow can be computed. An algebraic intermittency model was proposed by Dhawan & Narasimha [7], whereas a transport equation for intermittency γ was developed by Steelant & Dick [3,4,5,6] aiming to reproduce the γ-distribution function in the transition region. The original work of Steelant & Dick used two sets of conditionally-averaged Navier-Stokes equations, effectively doubling the computational effort and storage requirement. This limitation was removed by Suzen & Huang [8] who implemented a γ-transport equation, based on the models of Steelant & Dick and Cho & Chung [9], into a single set of RANS equations. A correlation-based transition model, only dependent on local flow variables and thus easily implementable in unstructured CFD solvers, was presented by Menter et al. [10] and Langtry et al. [11]. This model is built on the SST $k-\omega$ turbulence model and uses two additional transport equations for the intermittency γ and the transition onset momentum thickness Reynolds number $Re_{\theta,t}$. Van den Eynde & Steelant explored this avenue further by exploring the use of local empirical correlations on the basis of their γ-α model [13,14].

In this work, another approach is made through an a-posteriori prediction of the laminar-turbulent boundary layer transition point. A tool was developed and programmed in Python which detects and evaluates locally the boundary layer (BL) parameters of 3D CFD data. Subsequently, a set of empirical correlations for the transition point from the literature are evaluated based on the local boundary layer quantities. For a laminar input simulation the tool is then able to return surface maps for the different transition criteria showing where transition onset is predicted or even which critical roughness heights would trigger transition at any point on the surface

1. Transition correlations

The actual mechanisms of transition are complex and still not completely understood. The onset of transition as well as its progression is impacted by a whole set of different parameters such as free-stream conditions, pressure gradient, wall temperature, wall blowing/suction as well as surface roughness just to name a few.

Interested in a precise estimate of the transition point, a large experimental effort has been made so far to find transition correlations for super- and hypersonic applications. A selection of correlations is presented in the following sections. It has to be mentioned, that applying correlations derived from purely wind tunnel data on flight vehicles most likely leads to too conservative estimates for the transition point due to the acoustic noise of the tunnel. Also, as noted multiple times in literature, none of the correlations are able to collapse all of the available experimental data equally well, thus none of them can be regarded as universally applicable.

Basically, one can differentiate between correlations predicting the point of natural transition onset, the critical roughness height and the critical cavity dimensions. A brief selection of different transition correlations is presented below.

1.1. Natural transition onset

Actually investigating the optimisation of viscous waverider designs, Bowcutt et al. [15] correlated Eq. 1 from cone [16] and swept wing experiments [17]:

$$\log\left(Re_{x,tr}\right) = 6.421\exp(1.209\text{e}{-4}\,Ma_e^{2.641}) \tag{1}$$

In the NASP programme of the '80s, a transition criterion was found in the form of:

$$Re_{\theta,tr}/Ma_e = C \tag{2}$$

with originally $C = 305$ [18]. Other authors have fitted C to their data: Berry and Horvath [19] found C to be between 300 and 400 for the X-43A. Lau [20] uses a constant of $C = 318$ for sharp geometries, Bertin et al. [21] found C to be in the range of 110 to 162 for the shuttle orbiter while Berry and Horvath [19] found $C = 150$ and Thompson et al. [22] provided $C = 250$ for the windward centreline of X-33.

Simeonides [23] investigated transition at a flat plate under the influence of the leading edge bluntness. His correlation distinguishes between three levels of bluntness characterised by his bluntness Reynolds number Re_b which uses the leading edge thickness b as the characteristic length:

$$Re_{x,tr} = \begin{cases} 0.9\,Re_u/Ma_\infty & Re_b < 70\,Ma_\infty^{1.7} \quad \text{weak bluntness} \\ 70000\,Ma_\infty^{0.08}Re_b^{0.46} & Re_b < 1000\,Ma_\infty^{2} \quad \text{modest bluntness} \\ 6e6\,Ma_\infty^{1.38}Re_b^{-0.19} & Re_b > 1000\,Ma_\infty^{2} \quad \text{strong bluntness} \end{cases} \tag{3}$$

with the unit Reynolds number Re_u.

1.2. Critical roughness height

The roughness of a surface (e.g. affected by manufacturing tolerances) clearly has a big impact on the laminar-turbulent transition point. In the literature distinguished distinction is made between distributed roughness and discrete isolated roughness elements. Often, one can find slightly different definitions of a correlation depending on the context. The incipient value is defined as the one where the boundary layer remains laminar and just the smallest increase of the roughness Reynolds number would results in an earlier transition further downstream. The critical value is defined as the one where the flow downstream of the roughness element starts to be significantly transitional. Finally, the effective value is defined as the one where an increase in the roughness Reynolds number does not result in the transition moving upstream anymore because it is already anchored at or near to the roughness [24]. Unless otherwise stated, the following criteria are referring to the critical value.

1.2.1. Discrete Roughness

An early criterion for the discrete roughness height *k* is given by Braslow and Horton [25] as

$$\sqrt{Re_{kk}} = \sqrt{\frac{\rho_k U_k k}{\mu_k}} = 15 \ldots 30 \tag{4}$$

where the quantities building the Reynolds number have to be evaluated at the height of the roughness.

Investigating results of wind tunnel experiments on the influence of isolated roughness on the Space Shuttle orbiter, Berry et al. [26] found the correlation

$$\frac{Re_\theta}{Ma_e} = C\left(\frac{k}{d}\right)^{-1} \tag{5}$$

with the edge Mach number Ma_e and $C = 21$ for incipient and $C = 30$ for effective transition. Thompson et al. [22] note $C = 45$ for incipient and $C = 60$ for effective transition for C of Eq. 5 for the windward centreline of X-33.

King et al. [27] used historical flight and new wind tunnel data to present a second generation of transition correlations for NASA's BLT tool. One of their final proposals for discrete roughness induced transition reads

$$Re_{kk}^{0.6}\left(Re_\theta\frac{\mu_e}{\mu_k}\right)^{0.4} = C \tag{6}$$

using a C of 220.7 for incipient and 396.8 for effective transition.

1.2.2. Distributed Roughness

A PANT-like transition criterion is given by Reshotko and Tumin [28] for distributed roughness reads as

$$Re_\theta \frac{k}{\theta}\left(\frac{T_e}{T_w}\right)^{1.27} \tag{7}$$

1.3. Critical cavity dimensions

A cavity can be characterised by multiple geometrical parameters, e.g. the diameter, length or depth of the cavity. Based on the last one, the cavity depth, Berry et al. [24] and Horvath et al. [29] correlated STS-114 flight data with:

$$\frac{Re_\theta}{Ma_e}\frac{d}{\delta} = 100 \tag{8}$$

2. Functionality of the tool

The utility of the tool is the evaluation of correlations like those mentioned previously from a CFD solution of any generic 3D body. This requires knowledge about the local boundary layer in regards of (integral) boundary layer quantities as well as edge values and is reached in a three-step process: first wall-normal profiles are evaluated to detect the boundary layer locally, then the required boundary layer quantities are calculated and finally the transition correlations are evaluated.

Also, to give reasonable results for the transition area, the input simulation has to be a laminar one. Since the variety of CFD solver formats is large, it was decided to use the in ASCII written .dat format of Tecplot 360™, which most of the solvers are able to convert their results to, for input files. However, the latest tool version is currently still limited in supporting only 3D nodal data.

A second input file - a configuration file in .ini format - provides the interface between the user and the tool. The purpose of the configuration file is to identify certain variables of the simulation and guarantee consistency of variable names between simulation and tool, to define desired zones as walls for which the evaluation is done and to specify different options referring to the analysis part (e.g. a scaling factor so that the spatial coordinates are in meters).

Optionally, a third input file can be passed to the tool, which would be an Euler simulation of the same geometry as the viscous one's. The idea is to use the Euler wall velocity as an estimation of the locally expected velocity at the boundary layer edge. The concept of using the Euler simulation for the detection of the boundary layer edge is explained in more detail in Section 2.3.

2.1. Boundary layer characterisation

Besides the boundary layer thickness δ, other variables are also used to describe the local boundary layer or to model its state. These are on the one hand, integral quantities like the displacement thickness δ_1, the momentum thickness δ_2 or the energy thickness δ_3.

$$\delta_1 = \int_0^\delta \left(1 - \frac{\rho U}{\rho_e U_e}\right) dy' \tag{9}$$

$$\delta_2 = \int_0^\delta \frac{\rho U}{\rho_e U_e}\left(1 - \frac{U}{U_e}\right) dy' \tag{10}$$

$$\delta_3 = \int_0^\delta \frac{\rho U}{\rho_e U_e}\left(1 - \left(\frac{U}{U_e}\right)^2\right) dy' \tag{11}$$

To calculate these values, knowledge about the edge of the boundary layer in regards of δ but also the edge values of the velocity and the density is required plus the whole density and velocity profile up to this point must be available.

From these values, one can then calculate the two shape factors H_{12} and H_{32}:

$$\mathrm{H}_{12} = \delta_1/\delta_2 \tag{12}$$

$$\mathrm{H}_{32} = \delta_3/\delta_2 \tag{13}$$

On the other hand, one uses specific Reynolds numbers based on locally representative lengths. These can be e.g. the local distance to the attachment line or the momentum thickness:

$$\mathrm{Re}_\mathrm{x} = \rho_e U_e x/\mu_e \tag{14}$$

$$\mathrm{Re}_\theta = \rho_e U_e \theta / \mu_e = \rho_e U_e \delta_2 / \mu_e \tag{15}$$

The case of an incompressible, laminar boundary layer over a flat plate without pressure gradient is described exactly by the Blasius equation. Evaluating this equation for the boundary layer specific quantities leads to analytical solutions for the quantities in Eq. 9-15:

$$\delta = 5.0\,\mathrm{x}/\sqrt{Re_x} \tag{16}$$

$$\delta_1 = 1.7208\,\mathrm{x}/\sqrt{Re_x} \tag{17}$$

$$\delta_2 = 0.664\,\mathrm{x}/\sqrt{Re_x} \tag{18}$$

$$\delta_3 = 1.0444\,\mathrm{x}/\sqrt{Re_x} \tag{19}$$

$$\mathrm{H}_{12} = 2.591 \tag{20}$$

$$\mathrm{H}_{32} = 1.573 \tag{21}$$

For a supersonic laminar boundary layer over a flat plate, one can derive the following semi-empirical equations from the Blasius law:

$$\delta = \frac{\sqrt{x}}{\sqrt{Re_u}}\sqrt{C_w}\,(5 + 0.08 \cdot M_e^2 + 0.36 \cdot M_e^2 \frac{T_w}{T_e}) \tag{22}$$

with the Chapman-Rubensin parameter C_w, here evaluated at the wall:

$$C_w = \frac{\mu_w \rho_w}{\mu_e \rho_e} \tag{23}$$

$$\delta_1 = \left(2.591 + 0.667 \cdot M_e^2 + 2.9 \frac{T_w - T_{aw}}{T_e}\right) 0.664 \sqrt{\frac{\mu^* \rho^*}{\mu_e \rho_e}} \frac{x}{\sqrt{Re_x}} \tag{24}$$

$$\theta = 0.664 \sqrt{\frac{\mu^* \rho^*}{\mu_e \rho_e}} \frac{x}{\sqrt{Re_x}} \tag{25}$$

Eq. 24 and Eq. 25 use the reference values μ^* and ρ^* which are calculated as

$$\frac{\mu^*}{\mu_e} = \sqrt{\frac{T^*}{T_e}} \frac{1 + C_s/T_e}{1 + C_s/T^*} \tag{26}$$

with C_s being the Sutherland constant in this case, and

$$\frac{\rho^*}{\rho_e} = \frac{T_e}{T^*} \tag{27}$$

$$\frac{T^*}{T_e} = 1 + 0.54 \cdot \left(\frac{T_w}{T_e} - 1\right) + 0.16 \cdot \frac{\gamma - 1}{2} \cdot M_e^2 \tag{28}$$

2.2. Analysis of the velocity field

Via the configuration file, the tool can identify the data of the spatial coordinates, the velocity components as well as the temperature, pressure, density data. By specifying the wall zones there too, it can be distinguished between points in the fluid domain and wall points. For the latter, the tool first calculates the wall normal for each of them. Since the tool handles only nodal data, the wall normal at the vertex (where mathematically one cannot define a normal) is calculated by the average of the normals of the surrounding surface cells. The velocity boundary layer is then detected in a two-step approach utilising profiles normal to the surface: first, the edge of the boundary layer region is estimated roughly, then this region is resolved to provide a more precise result.

Therefore, a bounding box is created around the domain defined by the min. and max. values of each coordinate. For each wall point, the point of intersection of a wall-normal line with the bounding box is calculated. Subsequently, the distance to the wall point is equidistantly discretised with a specified number of points. Following this, the velocity components are interpolated for these profile points using a nearest neighbour interpolation. This returns the coordinates and velocities of the wall-normal profiles through the whole domain for every wall point. Additionally, the pressure is interpolated using a nearest neighbour interpolation as well.

At this point, a first profile evaluation in terms of an estimated boundary layer thickness is already possible. The according method assesses the BL thickness based on the generated profiles and is described in detail in Section 2.4.

Two different ways of the velocity profile evaluation exist: one uses the profiles of the velocity magnitude of all three velocity components and the other one just the wall-parallel components. The two variants can result in slightly different results, e.g. in the vicinity of the stagnation point of a blunt, supersonic body: while the velocity in the actual boundary layer is rather small, the wall-normal velocity component is large thus dominating the velocity magnitude. Therefore, detection of the boundary layer using just the magnitude of the wall-parallel components is also performed. The velocity is transformed into a local $x'y'z'$ system (see Fig 1) where x' and z' are wall-parallel and y' is wall-normal. While the y'-axis is already known, the x'- and z'-axis have to be calculated and are arbitrarily oriented.

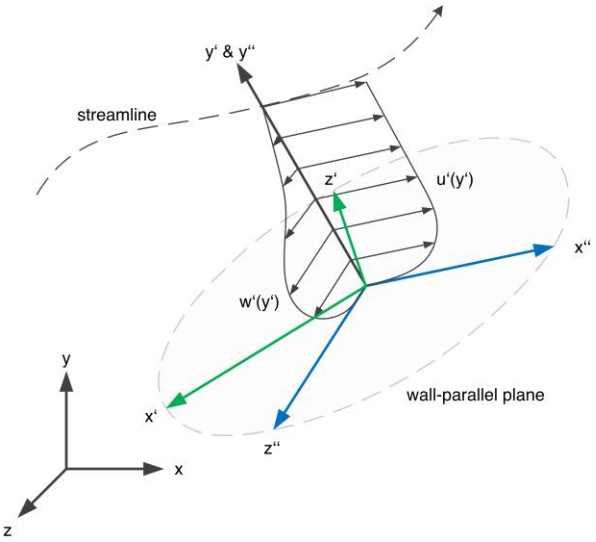

Fig 1. Three dimensional boundary layer profile with different coordinate systems

The just very rough estimation of the boundary layer is used to re-discretise the profile in this range providing a better resolution and to determine a more precise value for δ in a second evaluation using again velocity and pressure profiles.

Regarding the interpolation method of the profiles a nearest neighbour interpolation is used in the current version. While a linear interpolation would improve the quality of the results, the implementation via Delaunay triangulation did not always work flawlessly. Therefore the nearest interpolation was chosen due to simplicity and computational speed. This has to be paid with a rather poor quality of the profile, which is sufficient for estimating the boundary layer region but is not useable for an accurate detection of the boundary layer edge. Thus, the piecewise constant, nearest neighbour interpolated profiles are reconstructed to piecewise linear profiles (see Fig 2) for all required quantities before the evaluation, reducing the error to the original data.

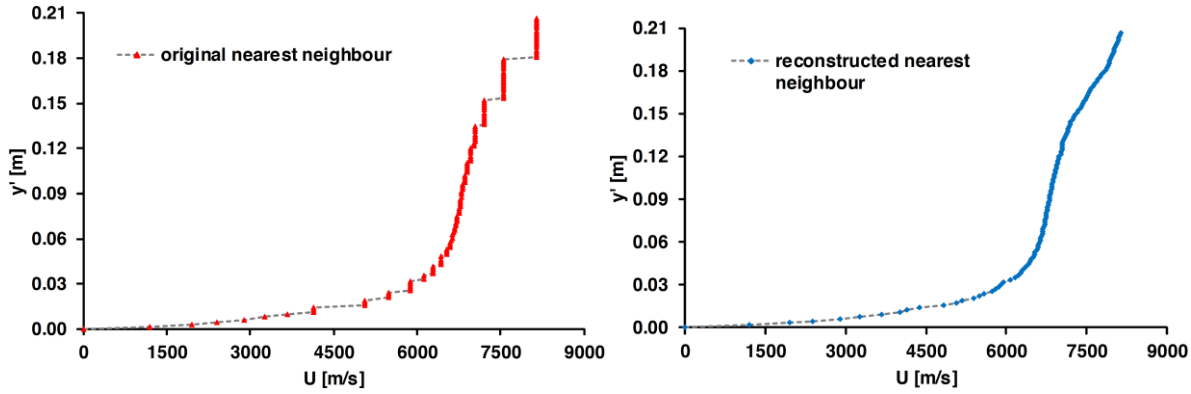

Fig 2. Generic nearest neighbour interpolated wall-normal profile

2.3. Auxiliary Euler simulation

Detecting the boundary layer for any arbitrary body can become very complicated and a local estimate of the expected boundary layer edge conditions would be helpful. One can think of taking an Euler simulation of the same geometry and using the Euler wall velocity for estimating the expected edge velocity in the Navier-Stokes solution. This option is implemented in the tool and can be used by simply providing the file of the Euler simulation as an additional third argument in the programme call. The provided Euler simulation has to be in the same units and scale as the viscous simulation with the same point of origin and the same direction of the coordinate axis. Like for the viscous simulation, the user has to provide certain information in the configuration file, so that the Euler simulations coordinate and velocity component variables can be identified. The latter are interpolated from the Euler mesh to the viscous simulation's mesh using a nearest neighbour interpolation. No further modification compared to the normal sequence of the programme exists besides that the Euler velocity can now be used for the detection of the boundary layer in the viscous simulation data.

2.4. Evaluation of the boundary layer

The algorithmic detection of the boundary layer is a primary part of the tool. Since the edge of the boundary layer is not always trivial to define for complex flows, a modular approach is implemented that is open for future modifications and extensions. This modularity is achieved by applying different detection criteria per profile which are then interrelated in a voting process where the importance of each criteria can be adjusted, finally leading to a local value for δ. The detection criteria are evaluated by using the velocity magnitude and pressure of the discretised profiles. While the velocity profile is used to determine the boundary layer thickness, the pressure profile is evaluated to avoid mistaking a shock for the boundary layer edge.

For each detection criterion a pseudo Boolean array with the size of the profile resolution is defined. It is initialized with zeros which means that the detection criterion is not fulfilled at the corresponding profile point. If the criterion is found to be fulfilled at a certain profile point during the evaluation process, the value will be changed to a one at the respective position in the array. The following criteria are used:

Criterion1: The point with the maximum of the velocity magnitude U_{max} within the profile is chosen. This criterion is used only if all other criteria fail in detecting a boundary layer edge.

Criterion2: Based on the definition of δ_{99}, the criterion is fulfilled for all points where the velocity magnitude exceeds $0.99\ U_{max}$ of the profile.

Criterion3: An ϵ-criterion for the first derivative of the profile which is fulfilled for $|\partial u/\partial y'| < \epsilon$. It can be seen as a criterion for the approximated vorticity assuming $rot(u,v,w)^T \approx = \partial U/\partial y'$. The ϵ-limit is calculated based on the derivative profile values itself which yields the advantage of being adjusted to the current profile. The ϵ-limit value is computed as the mean of two auxiliary values: *value1* is calculated as $|\partial u/\partial y'|_{min} + 0.3(|\partial u/\partial y'|_{max} - |\partial u/\partial y'|_{min})$ focusing on the number range and *value2* is calculated as three times the mean, absolute value of all derivative values which are less than *value1*, taking the distribution of the values into account. If the criterion is fulfilled by multiple points in a row, only the array value of the first one will be set to one while the others stay zero. Thus, only the positions in the profile where $|\partial u/\partial y'|$ drops below ϵ are saved.

Criterion4: In addition to the previous criterion, this one is based on the first derivative, too. For each of the points where the ϵ-criterion was fulfilled, the total variation of the first derivative of the following four profile points is calculated. Only the one with the lowest total variation fulfils the current criterion. The motivation for this criterion is that a boundary layer profile can have local maxima/minima due to disturbances. At these points the previous ϵ-criterion would be fulfilled as the discrete first derivative at extrema is around zero. For a local extremum, the derivative changes a lot in the following four points resulting in a high total variation while for the actual boundary layer edge, the derivative is expected not to change much anymore. Thus this criterion shall distinguish the boundary layer edge from local extrema.

Criterion Euler: If an Euler solution was provided in the function call an additional criterion will be evaluated. It is fulfilled by all points where the velocity magnitude of the viscous simulation is larger than 99% of the magnitude of the Euler simulation's interpolated wall-velocity.

Besides the criteria for the δ-detection there exists also a criterion for shock detection which is implemented as such a pseudo Boolean array called *requirementNoShock*, too. The one dimensional version of the Jameson-Schmidt-Turkel scheme [30] is implemented to detect possible shocks. The pressure based scheme calculates a shock indicator

$$\mathcal{I}_{JST,i} = \frac{p_{i-1}-2p_i+p_{i+1}}{p_{i-1}+2p_i+p_{i+1}} \tag{29}$$

which is done per profile point. Starting at the wall the local indicator value is compared with a critical one. This critical value is implemented as $5\mathrm{e}{-3}$ which was found to give quite good results in testing but cannot be considered universal. If the magnitude of the indicator value is smaller than the critical one, *requirementNoShock* will be set to one locally thus no shock is detected there. Else, the value stays zero and the comparison stops for this profile. All points of the profile where the requirement of no shock is not fulfilled are not taken into regard for the detection of the boundary layer edge. Due to this design decision, the boundary layer edge can only be detected below a shock even though physically it may be above.

A further variable *extFlowState* is used to adapt the detection criteria to the flow state at the boundary layer edge. It gives an estimate whether the flow there is rather homogeneous (like for a flat plate) or gradient dominated (like in a shock/entropy layer). If no shock in the profile exists, the outer 15% of the profile points are used as a data sample "*extFlowSample*" or else the 20% of the points before the shock are used. The value of the *extFlowState* is then set to a value between 0 (gradient dominated) and 1 (homogeneous) based on a case differentiation, see Eq. 31. The variable *DEFS* (deviation external flow sample) is introduced for readability.

$$DEFS = \frac{\max(extFlowSample)-\min(extFlowSample)}{\max(extFlowSample)} \tag{30}$$

$$extFlowState = \begin{cases} 1 & \text{if } U = 0 \text{ at any point in } extFlowSample \\ 1 & \text{if mean } \partial U/\partial y' \text{ for } extFlowSample < 0 \\ 1 & DEFS < 0.01 \\ 0 & DEFS > 0.04 \\ \frac{DEFS-0.01}{0.04-0.01} & 0.01 < DEFS < 0.04 \end{cases} \tag{31}$$

The first case aims for flows, where the profile reaches another wall at the end (e.g. internal flows or concave surface geometries). The second case is triggered for overshoots in the velocity profile. For such flows a typical δ_{99}-criterion is working well. Case three will be triggered for flows where the velocity gradient outside of the boundary layer is small. In contrast case four will be triggered, if there is still a velocity gradient outside of the boundary layer. Case five gives a linear blending for the region between case three and four.

Each criterion so far provided an array with the positions highlighted, where it detects possible boundary layer edges in the profile. These predictions are now combined in a voting procedure. In the variable *rating* one can define a formula which calculates a weighted rating value from the predictions of the single criteria. The current tool version uses the following rating formula:

$$rating = extFlowState \cdot Criterion2 + 0.55\,(1 - extFlowState)(Criterion3 + 0.5\,Criterion3LID) + 0.1\,(1 - extFlowState)(Criterion4 + 0.5\,Criterion4LID)$$

The variable *extFlowState* is used to adapt the criteria dynamically to the local conditions by multiplying it with the criterion arrays: For rather homogeneous outer flows only the classical δ_{99}-criterion is used while for gradient dominated flows the criteria based on the first derivative are applied.

Further, the criteria *Criterion3LID* and *Criterion4LID* appear in Eq. 32. These "*LID*" (local influence diffusion) criteria create a cross-influence between the criterion state of neighbouring cells for their according parent criterion: their state is set to one at the points before and after each point where the original criterion is fulfilled. This way it can be avoided that the *rating* value is small for a range where one criterion is fulfilled at position i and another criterion at position $i+1$. Due to the LID criteria the fulfilled criterion at i increases the *rating* at $i+1$ and vice versa. Thus the boundary layer is more likely detected in this region where two criteria are fulfilled.

The voting then chooses the profile point with the highest *rating* value to be the boundary layer edge. The according point index is backed up before the array *rating* is multiplied with the *requirementNoShock* array elementwise. The voting is then done again, using just the profile points below a possible shock (the ones above the shock are multiplied with zeros and consequently will not have the highest *rating* value). The according profile point is then the detected boundary layer edge. If there should be no result for the boundary layer edge after this step, the requirement array would be considered to be too strict and the backed up point would be chosen. If multiple points with the same highest value are found in the voting, the nearest one to the wall will be taken.

In case of a provided Euler solution, just the *Criterion Euler* instead of Eq. 32 is used.

This rather abstract procedure is demonstrated for a simplified example on a velocity profile consisting of only 13 points here, see Fig 3. One can note a shock at a height of around 0.02m. Fig 4 illustrates the corresponding voting process using generic criteria. As mentioned, the evaluation of the criteria is done per profile point and saved in arrays for each criterion. To the right, one can find the voting weights the single criteria are multiplied with. The dependency on *extFlowState* is depicted there, too. Also, a *LID* version of the third criterion is demonstrated. Its voting weight is set to a smaller value than the original's one. After the multiplication, the values are summed up pointwise (column-wise). The no-shock requirement is multiplied subsequently, removing the last two profile points from being eligible as the edge. From the final *rating* values the eighth point is determined as the boundary layer edge due to the highest value.

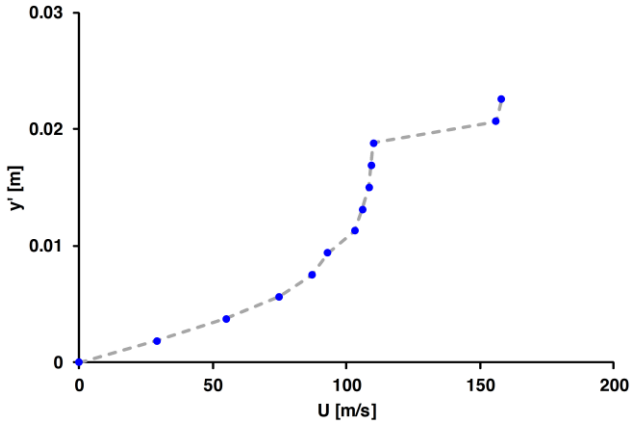

Fig 3. Generic wall-normal velocity profile

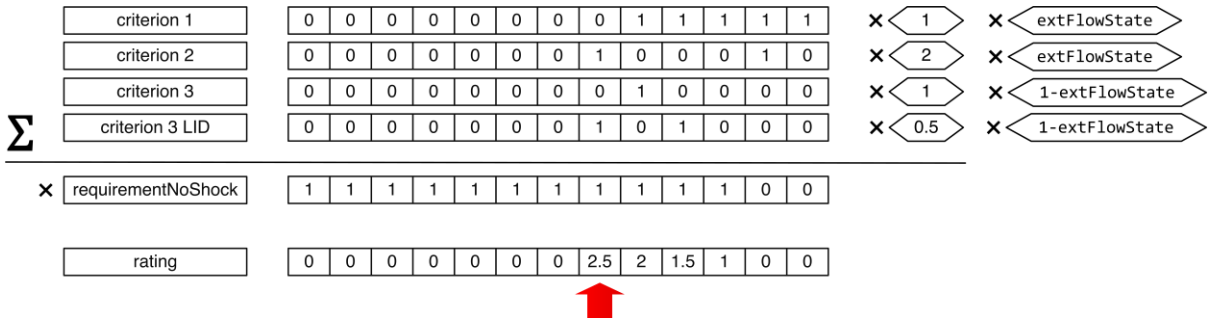

Fig 4. Exemplary schematic for the voting principle

2.5. Transition evaluation

With the knowledge of the local boundary layer edge all quantities required by the transition correlations can now be computed. The edge values of a quantity are the values of the quantity's wall-normal profile at the point index of the detected boundary layer edge. The integral boundary layer quantities δ_1, δ_2 and δ_3 are calculated using the trapezoidal rule for the points of the wall-normal profiles up to the detected δ. If a correlation uses a free-stream value of a quantity (e.g. Ma_∞ in Eq. 3), this value is actually taken at the local boundary layer edge for the implementation. The Mach number and dynamic viscosity can either be provided as a variable in the imported data or be computed by models: Ma will be calculated assuming a perfect gas using $c = \sqrt{\gamma\, R\, T}$ if γ and R are specified in the configuration file while μ will be calculated with Sutherland's law [31] if the model parameters μ_s, T_s, and C_s are provided in the .ini file. The only quantity which cannot be calculated yet is the local Reynolds number Re_x which some correlations rely on. While Re_x can easily be calculated for a flat plate, it becomes non-trivial for complex geometries. There, one has to take the local streamline length as the characteristic length of the Reynolds number. The algorithm for finding that length is explained in Section 2.6.

The criteria are then locally evaluated based on their context: for the natural transition a variable is returned with the values 0, where the resulting value is below the critical one, or 1, thus providing a laminar-transitional surface map. The criteria for critical roughness return a variable with the local critical values, which would trigger transition there, defined at the wall. For the implementation, the equations have been rearranged for k. Criteria, which use quantities like Re_{kk}, have to be evaluated at the local roughness height so that k appears implicitly in the correlation: one first has to know the critical height k, which is searched for, to determine where to take quantities like μ_k. Thus, the right-hand side of the equation, where all the k-dependent variables moved to, has to be calculated for every point in the wall-normal profile assuming the local height to be the critical one. Starting at the wall, this assumed critical value can then be compared to the actual wall-normal height of the current profile point. If the assumed critical value at the current height of the profile is larger, a roughness element of the current height in the profile would not trigger transition and the comparison is done for the next outer point in the profile. Else (the local critical value in the profile is lower than the current height) a roughness element of the size of the local wall distance would already trigger transition. Therefore, the distance of the previous profile point to the wall point is chosen to guarantee conservativity. Although one is able to evaluate such criteria for critical roughness or cavity dimensions with this method, the accuracy is limited to the resolution of the discretised wall-normal profile. As already noted, none of the criteria are universally applicable. It is up to the user to decide which of the criteria are sensible to use for the respective case and which of the resulting transition maps can be trusted.

2.6. Streamline length computation

To compute the local streamline length S, which is the length of the streamline from the leading edge to the current position, one first needs to identify the attachment line. Again, a criterion is used to detect the attachment line of an arbitrary body just from the provided data. The rationale is that δ is small at leading edges and therefore θ is small as well. Hence, the tool calculates the interquartile range of the overall momentum thickness distribution. Then, the upper outer fence of the distribution is calculated to reduce the scatter of falsely detected boundary layers without reducing the overall relevant value range. The points, which fulfil the empirical condition $\theta < \theta_{min} + 0.01(\textit{upper outer fence} - \theta_{min})$ with θ_{min} being the smallest, non-zero value of the momentum thickness in the whole domain, are classified as attachment lines.

The process of computing the local streamline length is explained using an example case: Fig 5 shows an unstructured surface mesh with the according point index of the cell nodes.

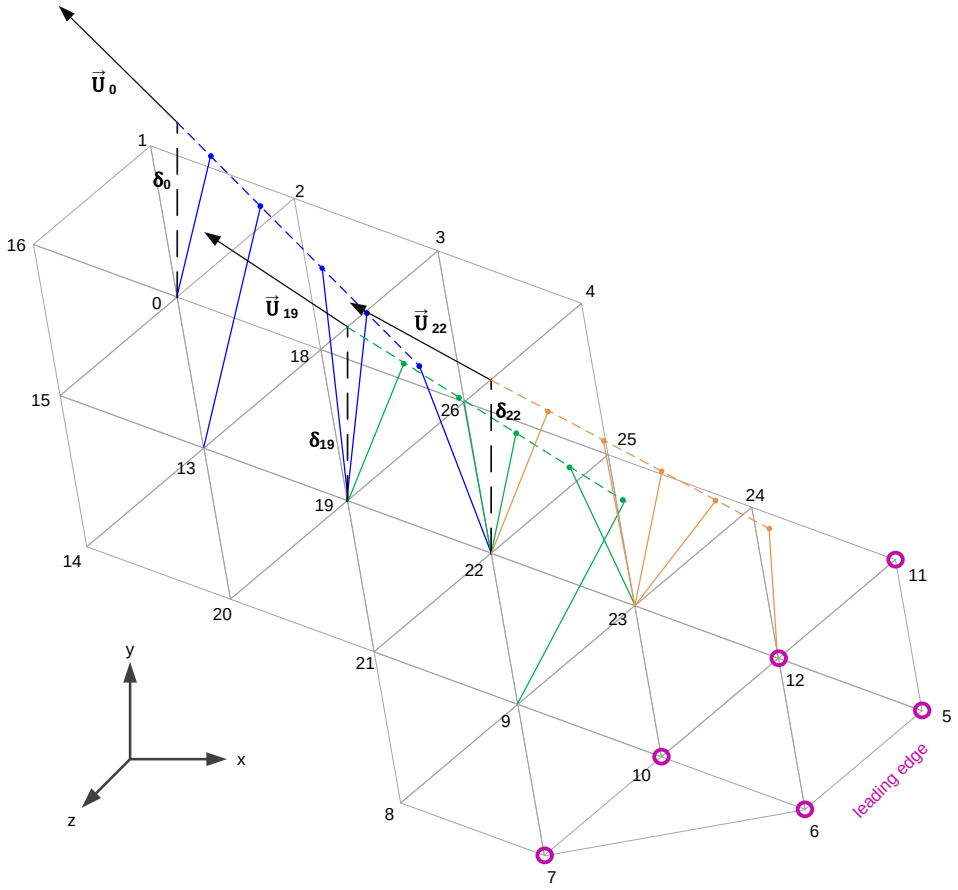

Fig 5. Schematic example of the streamline-length algorithm's operating principle

The algorithm starts with picking the first point with index 0, appending this index to a list called *wayOfStreamline* and building a line segment in upstream direction (dashed blue) at the edge of the detected boundary layer using the wall-parallel components of the velocity vector there. The length of this line segment is set to 5 times a characteristic cell length. This characteristic length is defined as the mean of the sum of the maximum distance between the nodes of the cell and the minimum of the distance from the current point to the previous or the next point in the cell - for all surrounding cells. The factor of 5 was arbitrarily chosen but worked very well: limiting the distance of the line segment, avoids going too far in upstream direction if the surface cells have a rather high aspect ratio. However, assuming the neighbouring surface cells to be approximately of the same size dimensions, the factor is still large enough to make sure that the line segment transcends at least one other surface cell in upstream direction. This line is then discretised with a small number (which is 10 in the implementation, but 5 in this example) of points (blue points). For these points, the point index of the actual mesh wall points is interpolated using a nearest neighbour interpolation. If one of these nearest wall points has the status of an attachment line, this point will be appended to the list *wayOfStreamline* and the function stops further reverse-tracing for the streamline. Else, the distance to the corresponding nearest wall point is calculated for each of the discretisation points (solid blue lines). The wall point which corresponds to the smallest distance – the initial wall point (here: index 0) excluded – is then chosen as the best fitting one (here: index 19) and appended to the list *wayOfStreamline*. The algorithm then repeats the procedure for the new wall point (green) like it has done for wall point 0 before. Taking now a new edge velocity vector the streamline curvature is comprised implicitly. For the example, the wall point with index 22 is found to be the best fitting in this second iteration and again appended to the list. In the third iteration (orange), one of the nearest wall points (index 12) is marked as an attachment line, defining the starting point of the streamline.

The list *wayOfStreamline* is then flipped (looking now [12,22,19,0]) and the variable *streamlineLength* is calculated for each of them. For wall point (WP) 12 the streamline length stays the initialised 0, for WP 22 the streamline length is the *streamlineLength* value of WP 12 plus the distance $\overline{W_{22}W_{12}}$ (with W for the wall point coordinates). Accordingly, for WP 19 the streamline length is the *streamlineLength* of WP 22 $+\overline{W_{19}W_{22}}$ and for WP 0 it is the *streamlineLength* of WP 19 $+\overline{W_0W_{19}}$. Before resetting *wayOfStreamline* and executing the procedure for the next wall point (index 1), the indices in *wayOfStreamline* are appended to another list which is used for efficiency reasons in further reverse-tracing: if a best fitting wall point (like the points 19, 22 in this example) are already appended to this list, the procedure will stop and the streamline length summation is done starting from this point, since a *streamlineLength* value was already calculated for this point. Also, for already processed points, the reverse-tracing is not started again, meaning that after calculating the streamline length for wall point 18, the function will skip wall point 19 since the streamline length is already calculated there.

Because the reverse-tracing is an iterative process, there is also a maximum number of 1000 steps defined. If this limit should be reached, the tool will use the streamline length from the wall point it started to the one it is in this moment. Also, it is possible that the velocity vectors points to a previous passed point which would cause a loop. Therefore the tool will stop the upstream-trailing as soon as it comes back to one of the wall points which were already passed in the upstream-trailing. One may argue that the distance calculated here is not the actual streamline length but the projected streamline length to the wall, which may differ slightly for curved surfaces. This is intended, as the correlations are all derived from experiments where Re_x is based on wall information. To detect transition, one often uses the increase of the wall heat flux, liquid crystal coating or other techniques at the wall thus making the Re_x dependent on the streamline distance at the wall. Still, the algorithm can just provide approximated values for the local streamline length because it just uses the best fitting wall-point as the next upstream point which in most cases is placed offside to the upstream extended velocity vector. Therefore, an error is introduced due to the simplification made by the algorithm.

The described process returns the length of the edge-streamlines but one can also use the wall-streamlines. Then the reverse-tracing of the streamline is based on the velocity vector in the second point of the discretised, wall-normal profile (which is the first point in the fluid as the first profile point is always identical with the wall point). The distance of this point is based on a set of different parameters (e.g. profile resolution, first estimation of the boundary layer, domain size) thus it is not a constant length for all profiles and the height where the velocity vector is taken might jump from wall point to wall point. Since there is no universal answer for the position where the streamline has to be evaluated, the user can set an according variable to take either the edge point or the wall-nearest point. The effect of the two different options on the results is presented in Section 3.2.2.

2.7. Further features

After the actual evaluation of the boundary layer and transition, the velocity profiles are transformed once more in another local coordinate system $x''y''z''$ illustrated in Fig 1, too. The difference to the $x'y'z'$ system is that the parallel but arbitrary aligned x'- and z'-axis are rotated around the y'-axis in such a way that the x''-axis is aligned with the boundary layer edge velocity vector projected to a wall-parallel plane afterwards. Thus, u'' points now in edgestreamline direction and w'' is the cross-flow component within the boundary layer. This enables the tool to detect separation by looking for negative u''-components in the velocity profile. For according profiles the height where u'' is larger than zero is saved as the *seperationThickness*. Also, the crossflow ratio $\max(|w''|)\,/|u_e''|$ can now be calculated per profile. Both variables are exported to the output data.

Finally, the reliability of the results is estimated by a function which detects nonsensible results or warns about possible problems. An according output variable *erroneousResults* is set to different values depending on the problem. This can be that the boundary layer is detected in the lowest 5% of the wall-normal profile so that the resolution of the actual boundary layer profile is considered as not sufficient. Also, if the boundary layer gets detected in the very outer part of the profile, the first estimate of the boundary layer might have been too low. Further, the boundary layer detection went wrong if the local displacement thickness is negative.

3. Validation

3.1. Laminar flat plate boundary layer

A comparison of the tool's results for a simulation of a laminar, quasi-2D flow over a flat plate of the length $L = 1m$ at $Ma_\infty = 0.3$ and $Re_u = 6.6e6\ 1/m$ and the analytical solutions given in Section 2.1 is depicted in Fig 6. The boundary layer thickness is well detected in the beginning but is overestimated downstream. However, the integral values do not suffer from this overshoot. The displacement thickness is predicted very well while the momentum thickness and energy thickness fit also well whilst a bit overestimated for the second half of the plate. This is further supported by Table 1 which lists the deviation of these quantities at discrete points along the plate. Also, the shape factors are around the values, one would expect from the Blasius solution.

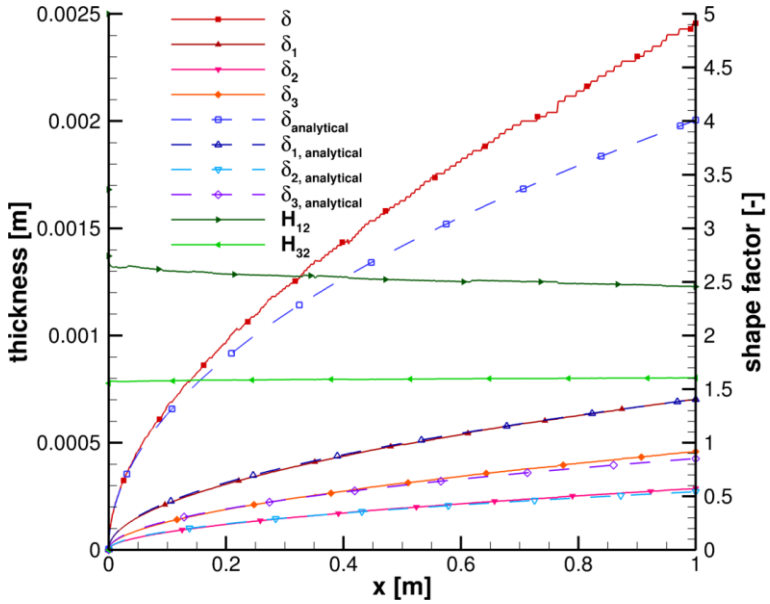

Fig 6. Comparison of tool detected BL quantities with analytical ones for a laminar flat plate

Table 1. Deviation of the tool detected boundary layer quantities to the analytical ones for the laminar flat plate

x [m]	0.1	0.2	0.3	0.4	0.5	0.6	0.7	0.8	0.9	1.0
$\Delta\delta$ [%]	9.72	11.63	14.25	16.58	18.29	19.98	21.66	22.91	24.69	26.22
$\Delta\delta_1$ [%]	2.25	2.51	2.84	3.31	3.93	3.51	4.5	4.64	4.85	4.99
$\Delta\delta_2$ [%]	1.81	3.22	4.24	5.18	6.94	7.12	8.04	9.21	9.89	10.73
$\Delta\delta_3$ [%]	2.12	3.94	5.35	6.48	8.26	8.69	9.77	11.17	11.97	12.92

While this comparison already proved that the general principle of the tool's boundary layer detection works, one has to note that the tool's detection cannot be any better than the simulation results provided. This means that the numerical solution does not necessarily has to agree with the analytical one since numerical schemes as well as the influence of the mesh impact the flow solution. A comparison between the tool's local, wall-normal velocity profile (orange) and the original profile extracted directly from Tecplot® (blue) is done in Fig 7 at two positions of the plate to examine this. One can note the excellent visual accordance between both profiles, which is also showing that the reconstruction from the original nearest neighbour data is worth the effort. The points where the boundary layer edge is detected is indicated by a green mark and seem to be reasonable for the presented profiles. Contrary to the impression from Fig 6, one cannot recognise a clear overestimation of the boundary layer thickness.

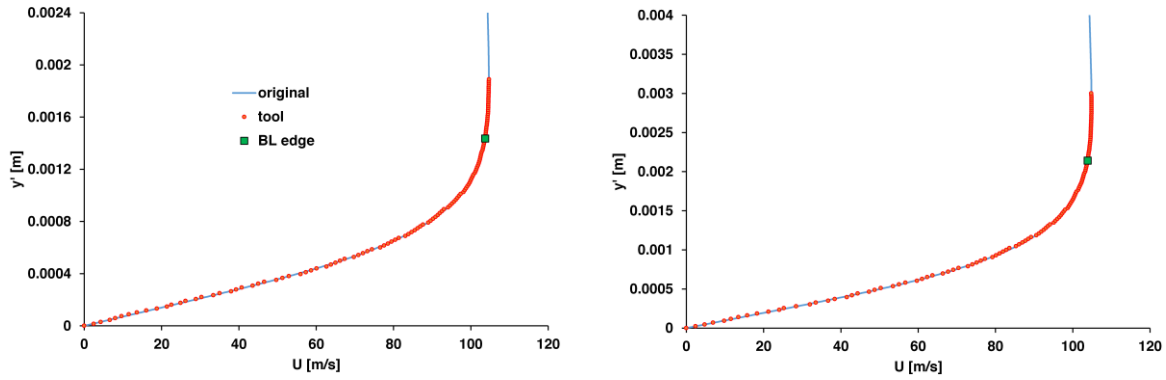

(a) $x = 0.4m$ **(b)** $x = 0.8m$

Fig 7. Comparison of the tool's velocity profile with the original one for a laminar flat plate

In Table 2, the deviation of the integral boundary layer quantities, calculated by the trapezoidal rule and using the discrete profiles, to the respective integral value of the exact profile is given for particular points. In both cases, the integration is done up to the detected boundary layer thickness making this a comparison of the integration and profile discretisation quality but not of the boundary layer edge detection itself. For all three quantities, the average deviation is below 0.25% for the evaluated profiles.

Table 2. Deviation of the tool detected boundary layer quantities to the ones from manually integrated Tecplot® profiles for the laminar flat plate

x [m]	**0.1**	**0.2**	**0.3**	**0.4**	**0.5**	**0.6**	**0.7**	**0.8**	**0.9**	**1.0**
$\Delta\delta_1$ [%]	0.05	0.10	0.13	0.11	0.42	-0.05	0.60	0.34	0.46	0.18
$\Delta\delta_2$ [%]	0.22	0.22	0.05	-0.35	0.37	0.01	0.11	0.23	0.43	0.27
$\Delta\delta_3$ [%]	0.16	0.22	0.07	0.29	0.26	0.02	0.13	0.28	0.50	0.28

3.2. Validation on EFTV

HEXAFLY-INT (High-Speed Experimental Fly Vehicle-International) is a project coordinated by ESA to promote research on civil high-speed air transport. It aims for a free flight experiment of a hypersonic glider, the European Flight Test Vehicle (EFTV), which is intended as a feasibility demonstrator for several technologies required for long-time hypersonic flight thus increasing the technology readiness level (TRL) of them. It will be launched with a sounding rocket on a suborbital trajectory having a hypersonic gliding phase of a few minutes in a height of 27 – 30km above ground then descending. Over 100 sensors will record inflight data, aiming for validation or improved understanding of transition, aerodynamic heating, structural stresses, shock-boundary layer interaction and flow separation at the flaps [32].

The HEXAFLY-INT aerodynamic design has been studied a lot with over 200 full 3D Navier-Stokes CFD simulations and intensive wind tunnel testing at the TsAGI T-116 wind tunnel facility [33,34] but also in a multidisciplinary context [35], resulting in a profound aerodynamic database. The tool's evaluation was applied to two different, fully laminar simulation cases, listed in Table 3. The results for the second case 243−01 are used to discuss the general outcomes while case 238−03 is used in Section 4.3 for a comparison with a transition estimation from literature**.** Both cases match to trajectory points at around 300 seconds after launch: case 238-03 (at 300.5s) is a simulation of the flight state 17 seconds after the separation from the Experimental Support Module (ESM), which controls the EFTV's attitude in the first phase of the descent phase, while case 243-01 is a simulation of the vehicle 9 seconds later.

Table 3. EFTV simulation case

Case ID	t **[s]**	Ma_∞	$Re_{u,\infty}$	AoA **[°]**	ϑ **[°]**
238-03	300.52	7.253	2.862e6	12	0
243-01	309.55	7.030345	3.73e6	1.63	0

3.2.1. Boundary layer profiles

Like for the flat plate case, wall-normal velocity profiles of the tool are compared to the profiles extracted from Tecplot® at particular positions. One can find a very good overall accordance between both profiles. Selected profiles are discussed in the following.

Fig 8(a) shows a velocity profile on the bottom side's centreline very near to the leading edge of EFTV's nose. One can recognise the shock at a height of around 0.2m normal to the wall. The shock detection worked correctly and therefore the edge is determined in the post shock region.

Fig 8(b) is taken exactly at the junction between the nose and the fuselage on the bottom of EFTV with an offset of $1m$ to the centreline. There, the boundary layer is not detected correctly, indeed the first point in the profile is already determined as the edge. Due to the geometry, an expansion fan is forming at this position which is effectively strong enough to trigger the shock detection and thus limiting the boundary layer to a value below the shock.

A correct detection of the boundary layer is shown in Fig 8(c), where one can find a more typical boundary layer profile at the upper centreline at around 40% of the vehicle's length.

A drawback of using the nearest neighbour interpolation can be found in Fig 8(d), where the tool's profile shows a strange step compared to the extracted one. The profile is taken quite close to the vertical stabilizer which is also illustrated in a slice of Fig 9. To follow the geometry, the prism mesh, which normally grows in wall-normal direction too and therefore keeps the error done by the nearest neighbour interpolation small, is now growing diagonal. In this case though, the nearest neighbour interpolation of the velocity profile first takes the values from the mesh nodes right to the wall normal. At a certain height (around $0.02m$), the values to the left side are closer and the interpolation switches to use them instead. Because the velocity on the left side is higher at the same distance to the wall, this causes the step in the profile. With a linear interpolation, this phenomenon is not to be expected.

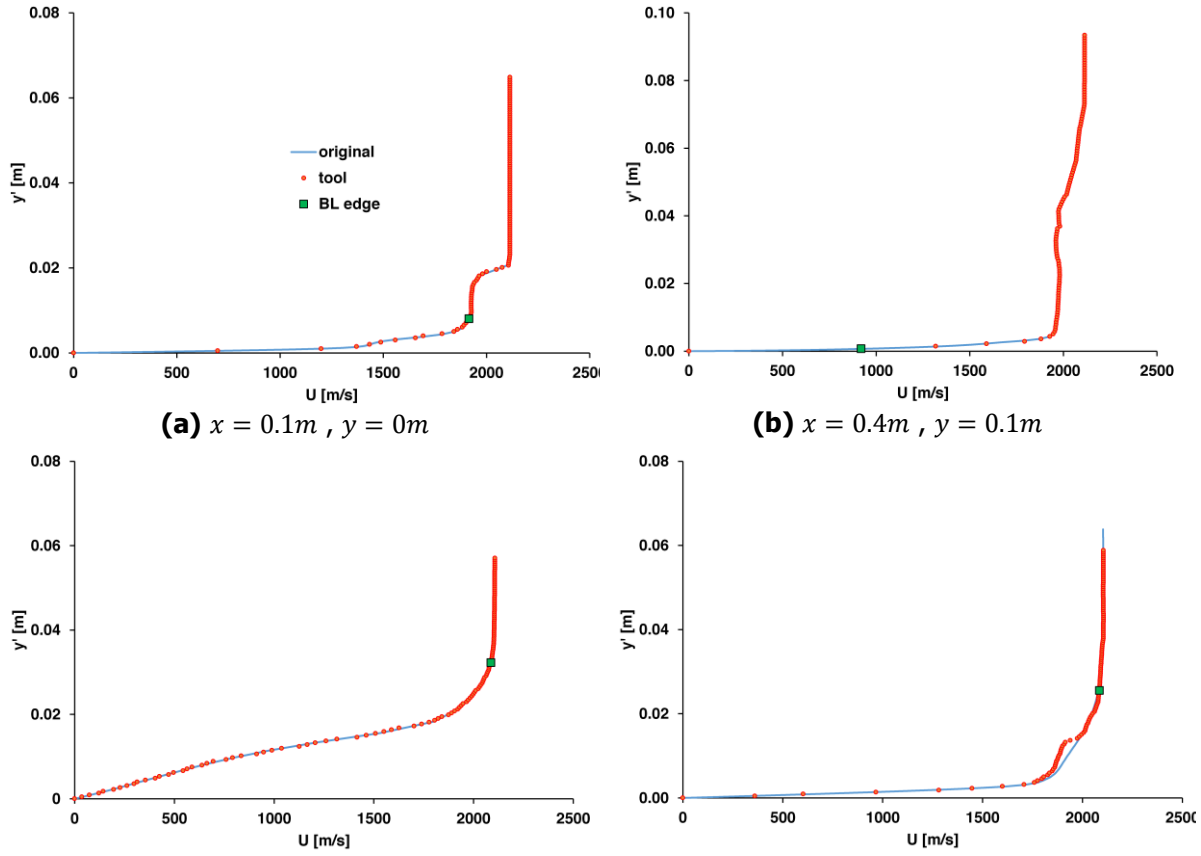

(a) $x = 0.1m$, $y = 0m$ **(b)** $x = 0.4m$, $y = 0.1m$

(c) $x = 1.4m$, $y = 0m$ **(d)** $x = 2.9m$, $y = 0.1m$

Fig 8. Velocity profiles at particular wall points of the EFTV

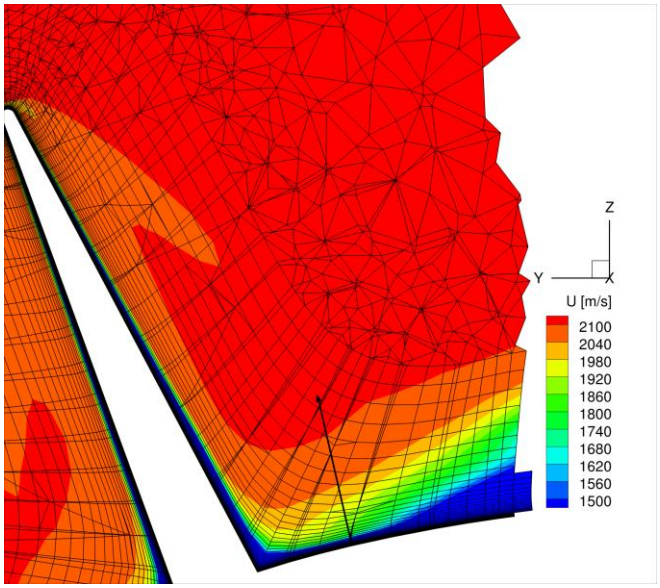

Fig 9. Slice at $x = 2.5m$ of EFTV

3.2.2. Streamline length

Fig 10 shows the results of the tool identified attachment line (red): the attachment line at the front and side part of the nose as well as at the leading edge of the wing and of the vertical stabilizer is detected correctly. However, some zones are detected as attachment areas falsely. On the one hand, this is the junction from the nose to the fuselage on the bottom side. There, the geometry leads to rather strong expansion fan which is also triggering the shock detection. Because the boundary layer is defined to be below the shock in the design of the tool, this restricts the boundary layer detection to a too small value and consequently a too small momentum thickness which then fulfils the criterion of the attachment line detection. On the other hand, one can note some erroneous spots on the upper wing and flap. For the spots close to the flap's trailing edge, this is due to a local separation zone which causes a wrong boundary layer detection.

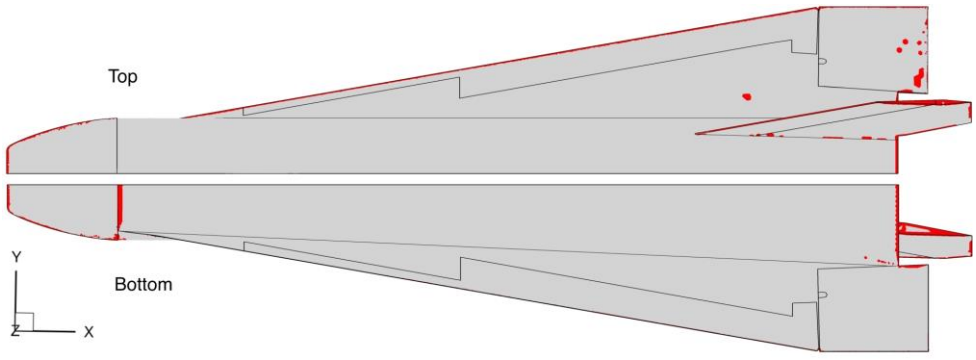

Fig 10. Attachment line determined by the tool's algorithm

Regarding the streamline length, the results of both methods - the length of the edge-streamlines and the one of the wall-streamlines - are plotted in Fig 11. Additionally, streamlines are shown at the boundary layer edge and near to the wall, respectively.

Looking at the computation for the edge-streamline in Fig 11(a), the streamline length at the top is homogeneously increasing in downstream direction. At the leading edge of the fin, the length restarts at zero and grows again. The results at the upper wing are adequate as well, although a bit spotted. One can recognise the influence of the wrongly detected leading edge zones, mentioned earlier. On the bottom however, the quality is strongly influenced by the wrongly detected attachment line at the junction between nose and fuselage. The reset of the streamline length, when passing this line, is clearly recognisable. The results at the lower wing are not impacted by this and are satisfying again. The value reached at the centre of the upper fuselage's trailing edge is 3.275m and the value on the

lower fuselage is 3.296m which is in good accordance with the 3.284m of the planar distance between nose and back.

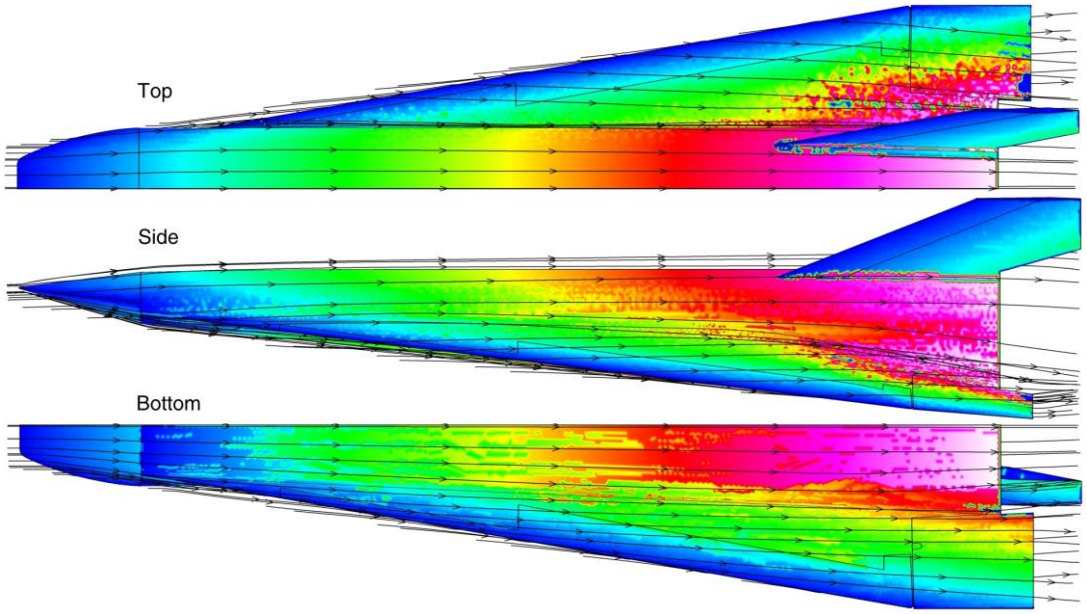

(a) edge-streamlines

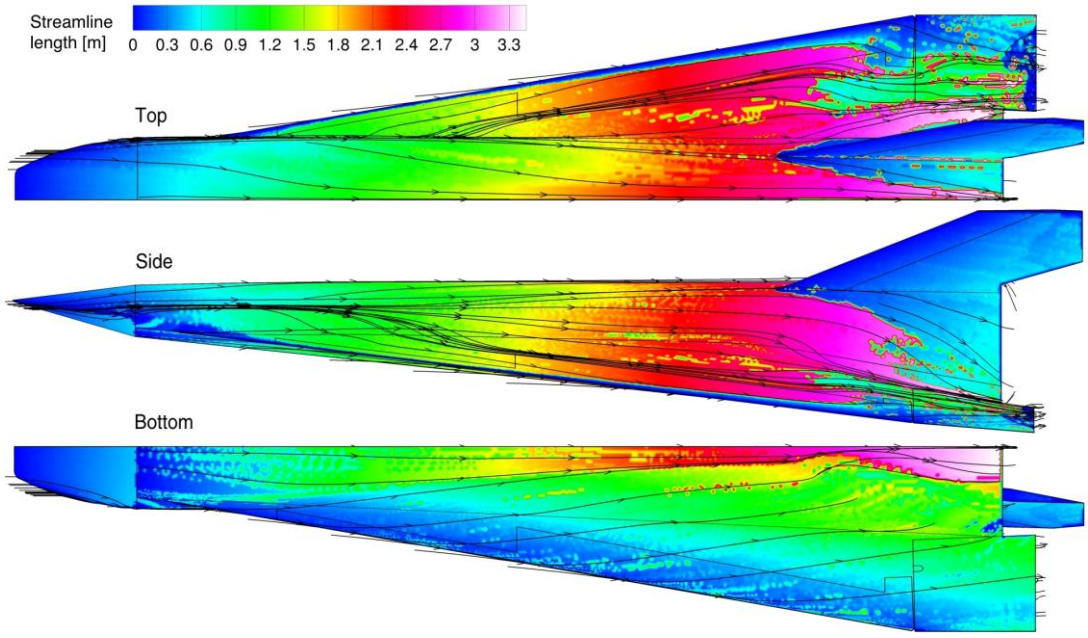

(b) wall streamlines

Fig 11. Streamline length depending on the used velocity vector in the profile

Fig 11(b) shows the evaluation based on the wall-streamlines. For the upper fuselage one can note, that the wall-streamlines from the side move towards the centreline. Because they attached not directly at the front part of the nose but further downstream at the side, the streamline length is lower than the one at the centreline position leading to a diagonal pattern. A big difference to edge-streamline length can be noted in the area around the vertical stabilizer. Due to the shock forming at the leading edge of the fin, the post-shock pressure is increased and the pressure gradient displaces the very wall-near boundary layer in normal direction to the edge-streamline. Since the velocity in this very wall-near zone is already subsonic, the angle of the influenced zone is even higher than the local Mach cone angle, perfectly shown in the side view and confirmed by the streamlines. At the back-part of the upper wing however, the streamlines have a wave-like shape. In this region the streamline length calculation returns wrong values for some reason. Looking at the bottom, one can detect again the reset of the streamline length at the nose-fuselage-junction as for the edge case. Different to the evaluation with

edge streamlines, the wall streamlines are moving towards the centreline downstream, making air, which attached at the wing, overflow the fuselage in the back-part.

Overall, the streamline length computation leads to qualitatively good results. The encountered problems mostly result from errors made by the attachment line detection. The accordance of the quantitative values at the centreline is acceptable keeping the approximative computation in mind. Also, the result is strongly influenced by where the velocity vector for the streamline analysis was taken.

4. Application

4.1. Boundary layer detection

In Fig 12 the detected boundary layer thickness using the described voting algorithm is plotted. The presented plot uses the boundary layer thickness which is detected by using just the wall-parallel velocity components. A difference to the detection using all three velocity components is just existent very occasionally and just at single wall points. Since the case presented here has a small angle of attack, one can already note the much smaller boundary layer thickness on the windward side of the EFTV. There, one can see the influence of the cross-flow within the boundary layer, noticed by the wall-streamlines in Fig 11(b), transporting boundary layer material from the wing towards the centreline of the fuselage. On the leeward fuselage, the boundary layer thickens for the same reason. Also, at the leeward side of the wing, the boundary layer thickening due to a local vortex structure is clearly visible.

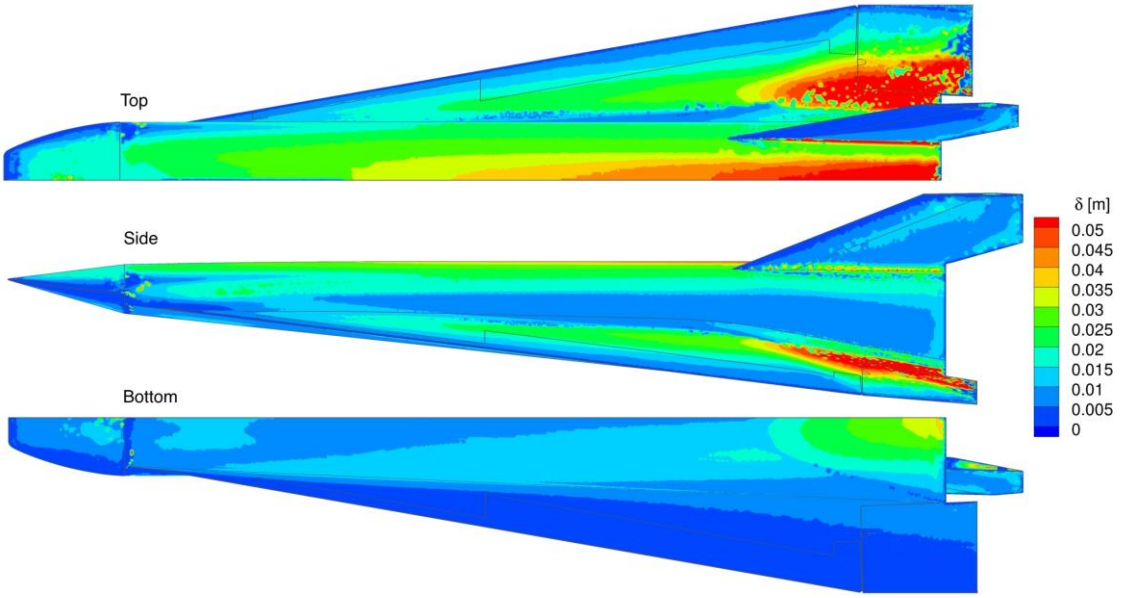

Fig 12. Boundary layer thickness mapped to the surface for EFTV

For the same case, the boundary layer thickness is depicted in Fig 13 but this time it is detected using an Euler simulation of the same mesh and boundary conditions. Thus, the boundary layer detection uses only the *Criterion Euler*. In direct comparison with Fig 12, one can note the very good accordance of the overall contour pattern, looking at the top and side view. The values differ slightly but especially in the nose region the Euler based boundary layer detection returns much smaller values for δ. One can also note that the results are less scattered using the Euler simulation.

However, for the bottom side, there is a big discrepancy to the voting detected result. While the boundary layer thicknesses at the wing are nearly identical, the second half of the lower fuselage shows an abrupt increase of the boundary layer thickness for the in the Euler based results. The reason for this is ambiguous. The effect might come from the missing displacement effect of the boundary layer in the Euler simulation leading to a quite different flow field. This would indicate that the detection with the Euler solution might not always lead to good results if used solely and could just effectively be used in combination with other criteria as part of the voting algorithm.

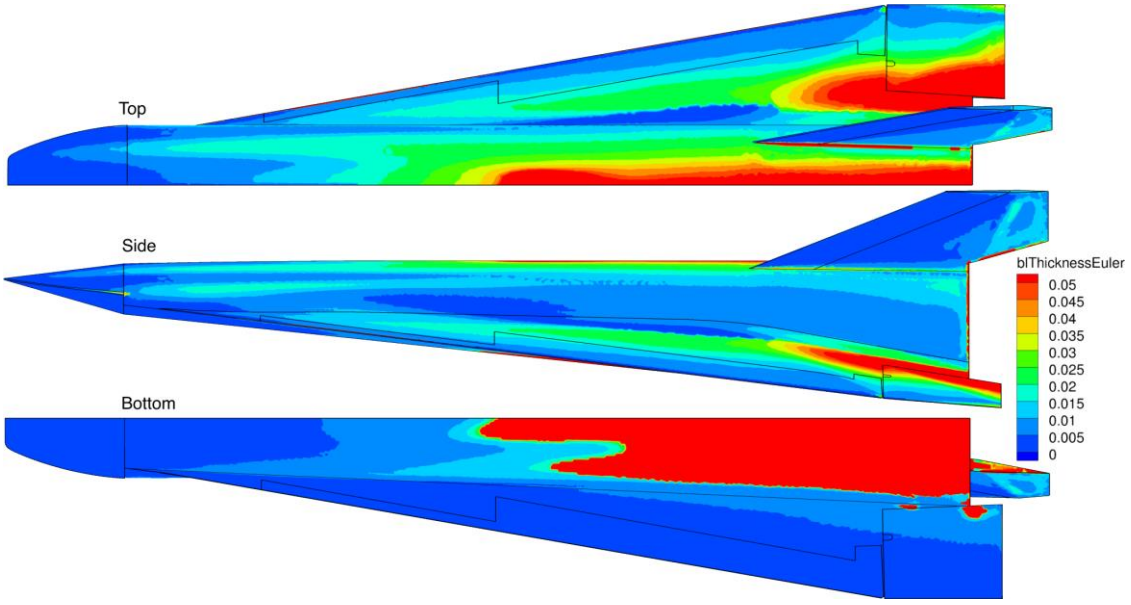

Fig 13. Boundary layer thickness detected by using the Euler wall velocity for EFTV

4.2. Integral boundary layer quantities

An example for the output of local, integral boundary layer quantities is shown in Fig 14 exemplarily for the momentum thickness since which is an often-used variable in transition correlations. The overall pattern looks similar to the one of the boundary layer thickness but appears to be smoother. While the detected boundary layer thickness may vary quite a bit, the change in the integral value is not that significant because the gradient in the outer part of the profile is already small compared to the wall-near one. Hence, the scatter of the boundary layer thickness does not propagate to the integral values.

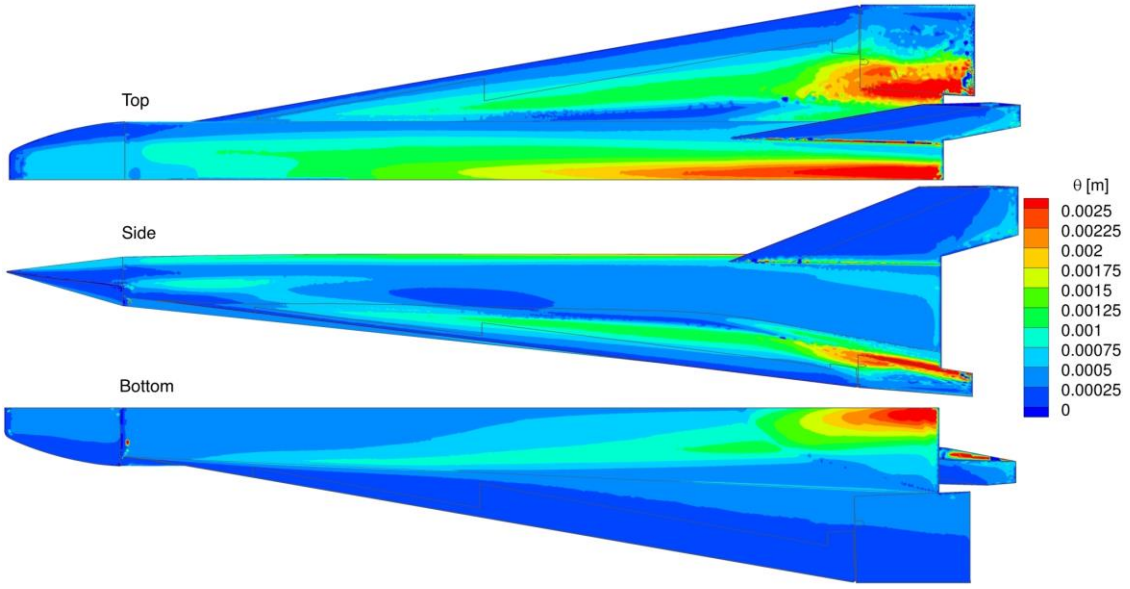

Fig 14. Momentum thickness mapped to the surface for EFTV

4.3. Transition analysis

Two exemplary surface plots shall demonstrate the final transition results: Fig 15 shows the surface map of the simulation case 243−01 using the NASP criterion: blue colour indicates laminar flow while red colour means transitional flow. Some transitional spots are detected already at the nose but one can argue that this is due to difficulties with the boundary layer detection in this area. However, transition of the flow is predicted to establish at the centreline of the upper fuselage at around 50% of the vehicle length. On the bottom side, transitional flow is predicted in the area of the already noted cross-flow influence between wing and fuselage. In Fig 16, the critical roughness height k according to

the criterion by Thompson et al. (Eq. 5) is depicted. Since the boundary layer is much smaller on the windward side due to the effect of the small angle of attack and the overall vehicle design, k is notably smaller there. The critical roughness height is detected as very large at the leading edges which is somewhat expected. Indeed, tripping a fresh, thin boundary layer is pretty difficult in practice. This also results from the applied criterion which is actually proportional to $1/Re_\theta \propto 1/\theta$ at the location where the momentum thickness is very small there.

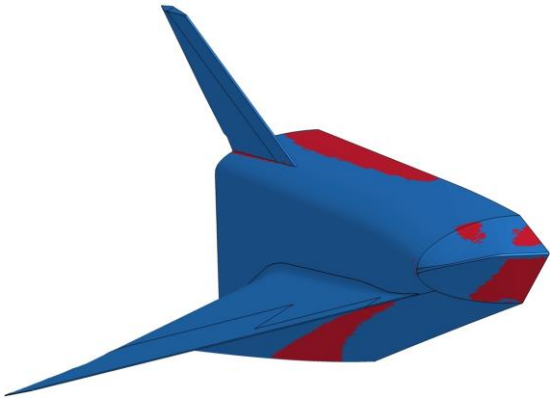

Fig 15. Transition map of the NASP criterion with $C = 400$ applied to 243-01

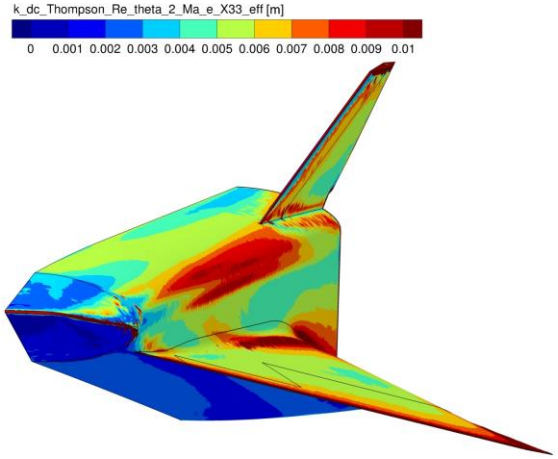

Fig 16. Critical roughness height map for 243-01 based on Thompson et al.'s criterion

Finally, this section compares the transition assessment based on correlations and wind tunnel experiments published by Steelant et al. [36] with the results of the same correlations using the tool applied to an according simulation. Therefore, one of the investigated flight trajectory cases, EFTV−069, from the publication was compared with the simulation case 238−03 matching in Mach number, Reynolds number and AoA (see Table 3).

For the transition point, the criterion of Bowcutt et al. (Eq. 1) which is referred to as the criterion of Di Cristina there, the NASP-criterion (Eq. 2) with $C = 400$, and the correlation of Simeonides (Eq. 3) were used. Also, a correction for the sweep angle Λ of the wing was used for the criterion of Bowcutt there:

$$\frac{Re_{x,tr,\Lambda}}{Re_{x,tr,\Lambda=0}} = 0.787\cos(\Lambda)^{4.346} + 0.7221\exp(-0.0991\Lambda) + 0.9464 \tag{33}$$

Regarding roughness induced transition, two criteria were used for evaluation. For two dimensional steps, the criterion Eq. 5 was applied using a constant $C = 344.45$ for backward facing steps. A criterion for Görtler vortices induced by these 2D steps is also given as:

$$k/\delta = 2 \tag{34}$$

4.3.1. Transition onset

The outcome of the correlation based estimation of the transition onset can be found in Table 4 and Table 5 for the fuselage and the wing. The transition point is given there in regards of the x-coordinate, which has its point of origin at the junction between nose and fuselage. For the correlation of Simeonides a leading edge radius of $2mm$ at the nose and $1mm$ for the wing is used.

Table 4. Estimation of transition onset at the centreline of the fuselage for EFTV − 069 [36]

Criterion	windward	leeward
Simeonides	$x = 1.36m$	no transition
Bowcutt et al.	no transition	no transition
NASP	$x = 1.9m$	no transition

Table 5. Estimation of transition onset at the wing ($y = 0.47m$) for EFTV – 069 [36]

Criterion	windward	leeward
Simeonides	no transition	no transition
Bowcutt et al.	no transition	no transition

Compared to the previous simulation case 243–01, this one is much harder for the tool. Due to the higher angle of attack, the shock on the windward side is much stronger and the whole flow field behind it is affected by gradients. Indeed, for $x > 0.88m$ the boundary layer is detected as too big thus making downstream results on the fuselage not trustworthy. The same occurs at the outer part of the wing for $x > 0.3m$. On the other hand, on the windward side a lot of vortex structures are forming at both the wing and the fuselage, which influence the boundary layer detection, too. The influence of these secondary flows on transition was also noted by Steelant et al. in wind tunnel experiments conducted with a 0.35 scale model at $Ma = 6.99$ and $Re = 8.82\text{e}6$ with an AoA of also $12°$. The predicted positions for transition onset of the tool can be found in Table 6 and Table 7. The results confirm the absence of transition at the leeward side. The NASP criterion results shows a small transitional streak after the nose from $0.3m$ to $1.3m$, which might be due to a vortex structure there. On the windward side, the criterion of Simeonides predicts a later and the NASP criterion an earlier transition compared to the values in [36]. The criterion of Bowcutt et al. predicts transitional flow at around the position where the boundary layer edge is detected wrongly. For the wing, the same criterion with the swept angle correction applied predicts no transition while the criterion by Simeonides predicts transitional flow at the end of the wing.

Table 6. Tool results for transition onset at the centreline of the fuselage for EFTV–069

Criterion	windward	Leeward
Simeonides	$x = 1.63m$	no transition
Bowcutt et al.	$x = 0.88m$	no transition
NASP	$x = 1.3m$	$(x = 0.3 \dots 1.3m)$

Table 7. Tool results for transition onset at the wing ($y = 0.47m$) for EFTV–069

Criterion	windward	leeward
Simeonides	$x = 2.7m$	no transition
Bowcutt et al.	no transition	no transition

4.3.2. Critical roughness

Using the earlier mentioned criteria, "[...] the maximum step heights allowed to avoid triggering earlier transition [...]" [36] found in the publication is given by Table 8 and Table 9 for different positions in x-direction. The data given there is just for the criterion for 2D steps and Eq. 34.

Table 8. Estimation of critical roughness height k at the centreline of the fuselage for EFTV–069 [36]

x [m]	0.0	0.5	1.0	1.5	2.0	2.5	side
BFS	3.7mm	6.3mm	5.6mm	5.6mm	5.3mm	7.4mm	windward
Görtler	5.3mm	9.4mm	10.8mm	12.5mm	13.8mm	17.1mm	
BFS	67.3mm	65.1mm	56.0mm	55.8mm	57.9mm	59.7mm	leeward
Görtler	19.2mm	27.4mm	31.6mm	37.3mm	43.0mm	47.7mm	

Table 9. Estimation of critical roughness height k at the wing ($y = 0.47m$) for EFTV – 069 [36]

x [m]	2.0	2.5	2.75	side
BFS	4.5mm	4.7mm	18.8mm	windward
Görtler	4.3mm	7.3mm	16.2mm	
BFS	70.7mm	122.9mm	37.0mm	leeward
Görtler	16.4mm	35.6mm	23.1mm	

In Table 10 and Table 11, the tool's results at the corresponding positions are given. For the windward side, one can clearly see the influence of the overestimated boundary layer for $x > 0.88m$ at the fuselage mentioned earlier. The results of the Görtler criterion are about an order of magnitude larger than the one by Steelant et al. For $x = 0m$, the result is irrational wrong, too, due to the triggered shock indicator by the rather strong expansion fan. Only for $x = 0.5m$, no error is made and the results is in acceptable accordance with the values given by Steelant et al.. The wing results also suffer from a too thick detected boundary layer. Regarding the leeward fuselage's centreline, the accordance is good for $x = 0.5m$ and $x = 1.0m$. For $x > 1.5m$ the results differ by factor two which is probably due to the secondary flow structures there. For the leeward wing side, the results also show no good agreement. This is again probably due to the vortex structure forming there, which influences the boundary layer detection leading to different values compared to Steelant et al.

Table 10. Tool results for k at the centreline of the fuselage for EFTV−069

x [m]	0.0	0.5	1.0	1.5	2.0	2.5	side
BFS	-	8.8mm	59.0mm	32.3mm	17.5mm	18.5mm	windward
Görtler	1.8mm	10.1mm	78.3mm	95.6mm	100.0mm	92.5mm	
BFS	97.1mm	91.0mm	68.4mm	109.6mm	125.7mm	119.6mm	leeward
Görtler	7mm	196.4mm	340.5mm	38.0mm	27.4mm	21.2mm	

Table 11. Tool results for k at the wing ($y = 0.47m$) for EFTV – 069

x [m]	2.0	2.5	2.75	side
BFS	13.4mm	14.7mm	14.9mm	windward
Görtler	19.5mm	34.3mm	39.4mm	
BFS	124.9mm	179.4mm	269.3mm	leeward
Görtler	52.0mm	109.9mm	83.6mm	

4.4. Discussion on the results' quality

First, it has to be noted that the overall concept of the tool still works well then applied to a complex, 3D geometry and flow field. This proves the strong potential of the developed methods and algorithms. The quality of the results strongly depends on the quantity of interest. Through the discretisation in the boundary layer detection process, the tool is limited to a certain step-size between the profile points by its design.

While for flat plates a δ_{99}-criterion of the highest velocity in the profile works fine, the detection and even the definition of the boundary layer edge becomes difficult for the more complicated boundary layers. For the integral boundary layer values some accuracy is lost because the tool integrates from the wall to the potentially error-prone boundary layer thickness (propagated error) using the trapezoidal rule on a discretised profile (discretisation error). Calculating further quantities like Re_θ, one has to multiply with the edge values which are again depended on the potentially error-prone boundary layer

thickness. In the transition correlations, multiple of these quantities are then added, multiplied and divided with each other, increasing the error. This however should mostly not matter since most of the empirical correlations were fitted with a ±20% uncertainty.

Although some of the errors are actually rather small, like the one done by the integration or the edge conditions there are a larger ones. Evaluating roughness criteria, where the flow quantities have to be taken at the roughness height like Re_{kk}, is one of them. As explained in Section 2.5 the accuracy of the predicted roughness height is limited to the step size of the profile discretisation. For Re_x, the value is less reliable because it depends on the streamline length. Fig 11 showed that areas exist where this value is calculated incorrectly.

Lastly, the application to EFTV−069 showed that the boundary layer detection is still no perfect. Although a universal voting formula of the boundary layer detection criteria would be preferable, the user might want to adapt the formula according to the simulation case.

4.5. Future features

One can identify potential for improvement by using the linear interpolation for the generation of profiles. Besides their better quality, this would also enable new possibilities for the boundary layer detection i.e. one could use criteria based on the profiles' second derivative, too. One can further improve the sequence of the boundary layer detection for a more general application. In the current version, the detection is performed in two steps first estimating and then resolving the boundary layer. This is well working for hypersonic applications where the far-field does not need to be large since the influence of the local flow state is not global but limited to the Mach cone. For other applications, the far-field can be quite far away from the geometry. This would lead to a drastic loss in precision because the fixed number of profile points is now distributed over an increased profile height. To avoid this, one could introduce an iterative procedure, which ensures a sufficient resolution of the boundary layer by resolving it until at least e.g. 50% of the profile points are below the detected edge.

Regarding the transition analysis, one can think of different extensions. One can compute further parameters like the pressure gradient in streamline direction allowing to implement even more correlations from literature. Also, correlations for transition mechanisms which were not treated in this work, e.g. the attachment line transition at swept wings, could be implemented. Furthermore, one could add the prediction of unsteady transition dependent on a frequency which would be a parameter the user has to specify in the configuration file. Another aspect would be to estimate not only the transition point but also the extent of the transitional area. Lastly, the tool's transition maps could be used for simulations with intermittency based transition models (e.g. γ -$Re_{\theta,t}$ or γ-α).

In addition, a local evaluation of other onset mechanisms, e.g. the onset of catalycity of the wall or the onset outgassing of an ablative surface material would be conceivable.

5. Conclusion

A tool was developed that can analyse laminar-turbulent transition on complex 3D geometries by applying empirical correlations on a laminar solution. Because this requires knowledge of local boundary layer quantities, an analysis of the velocity field is performed first. The boundary layer edge is determined by evaluating discretised wall-normal profiles using different "edge determination" criteria in a voting-based algorithm. Integral boundary layer quantities like the momentum thickness are then locally computed. Furthermore, the tool is capable of detecting attachment lines and calculating an approximated streamline length from the attachment line to the local surface position. With the knowledge of the local, characteristic boundary layer variables as well as the boundary layer edge values and the local streamline length, the criteria for transition can be evaluated. The implemented correlations subdivide into criteria for transition onset, criteria for the critical roughness height and criteria for critical cavity dimensions.

The tool's evaluation is saved to an output file of the same format as the input file, Tecplot®'s .dat format, which contains the original provided data, the local boundary layer quantities and the results from the transition assessment. The latter are saved as a new variable per criterion which can either have a Boolean transition state (laminar-transitional) or the critical sizes of a roughness element and cavity, respectively and which is just defined at the surfaces of the geometry. The tool further provides useful features like the detection of boundary layer separation or the crossflow-ratio.

The functionality of the tool was validated in flat plate test cases for a laminar boundary layer and showed satisfying accordance. The tool then was applied to simulations of the EFTV and compared to published transition estimation data for the same conditions. The accordance on the leeward side was good taking into account the vortex structures locally influencing the results. For the windward side the accordance was not as good due to reliability of the boundary layer edge detection.

Although certain aspects of the tool need to be extended or improved, the current version already provides a sound basis for a-posteriori transition and boundary layer analysis.

Acknowledgements

This paper is based on the first author's master's thesis which was conducted within the HEXAFLY-INT framework. In this context the authors want to thank Prof. Jens von Wolfersdorf for his contribution and making this work possible. In addition the authors want to thankfully mention the provision of simulations by Dr. Victor Fernandez Villace.

References

1. NASP Task Force. Report of the Defense Science Board Task Force on the National Aerospace Plane (NASP). Technical report, Defense Science Board, Office of the Secretary of Defense, Washington, D.C. 20301-3140, AD-A201124 (Sept. 1988)
2. NASP Task Force. Report of the Defense Science Board Task Force on the National Aerospace Plane (NASP). Technical report, Defense Science Board, Office of the Secretary of Defense, Washington, D.C. 20301-3140, AD-A274530 (Nov. 1992)
3. Steelant, J., Dick, E.: Modelling of Bypass Transition with Conditioned Navier-Stokes Equations Coupled to an Intermittency Transport Equation. International Journal for Numerical Methods in Fluids 23, 193–220 (1996). https://doi.org/10.1002/(SICI)1097-0363(19960815)23:3%3C193::AID-FLD415%3E3.0.CO;2-2
4. Steelant, J., Dick, E.: Prediction of By-Pass Transition by Means of a Turbulence Weighting Factor - Part I: Theory and Validation. ASME paper 99-GT-29 (1999). https://doi.org/10.1115/99-GT-029
5. Steelant, J., Dick, E.: Prediction of By-Pass Transition by Means of a Turbulence Weighting Factor - Part II: Application on Turbine Cascades. ASME paper 99-GT-30 (1999). https://doi.org/10.1115/99-GT-030
6. Steelant J., Dick, E.: Modeling of Laminar-Turbulent Transition for High Freestream Turbulence. J. Fluids Eng. 123(1), 22-30 (2001). https://doi.org/10.1115/1.1340623
7. Dhawan, S., Narasimha, R.: Some properties of boundary layer flow during the transition from laminar to turbulent motion. J. Fluid Mech. 3(4), 418-436 (1958). https://doi.org/10.1017/S0022112058000094
8. Suzen, Y.B., Huang, P.G.: Modeling of flow transition using an intermittency transport equation. J. Fluids Eng. 122(2), 273–284 (2000). https://doi.org/10.1115/1.483255
9. Cho, J.R., Chung, M.K.: A k-ε-γ equation turbulence model. J. Fluid Mech. 237, 301-322 (1992). https://doi.org/10.1017/S0022112092003422
10. Menter, F.R., Langtry, R.B., Likki, S.R., Suzen, Y.B., Huang, P.G., Völker, S.: A Correlation-Based Transition Model Using Local Variables – Part I: Model Formulation. J. Turbomach. 128(3), 413-422 (2006). https://doi.org/10.1115/1.2184352
11. Langtry, R.B., Menter, F.R., Likki, S.R., Suzen, Y.B., Huang, P.G., Völker, S.: A Correlation-Based Transition Model Using Local Variables – Part II: Test Cases and Industrial Applications. J. Turbomach. 128(3), 423–434 (2006). https://doi.org/10.1115/1.2184353
12. Chazot, O., Gülhan, A., Hannemann, K., McGillvray, M., Serre, L., Tran, Ph., Steelant, J.: Need for Low-Noise High-Speed Facilities in Europe. 1st International Conference on Flight vehicles, Aerothermodynamics and Re-entry Missions and Engineering (FAR) (2019)

13. Van den Eynde, J., Steelant, J., Passaro, A.: Intermittency-based Transition Model with Local Empirical Correlations. 21st International Space Planes and Hypersonics technologies Conference (2017). https://doi.org/10.2514/6.2017-2378

14. Van den Eynde, J., Steelant, J.: Two-Equation Transition Model Based on Intermittency and Empirical Correlations. 1st HiSST: International Conference on High-Speed Vehicle Science & Technology (2018)

15. Bowcutt, K.G., Anderson, J.D., Capriotti, D.: Viscous Optimized Hypersonic Waveriders. AIAA 25th Aerospace Science Meeting (1987). https://doi.org/10.2514/6.1987-272

16. DiCristina, V.: Three-Dimensional Laminar Boundary-Layer Transition on a Sharp 8° Cone at Mach 10. AIAA J. 8(5), 852–856 (1970). https://doi.org/10.2514/3.5777

17. Pate, S.R., Groth, E.E.: Boundary-Layer Transition Measurements on Swept Wings with Supersonic Leading Edges. AIAA J. 4(4), 737-738 (1966)

18. Berry, S.A., Auslender, A. H., Dilley, A. D., Calleja, J. F.: Hypersonic Boundary-Layer Trip Development for Hyper-X. J. Spacecr. Rockets 38(6), 853–864 (2001). https://doi.org/10.2514/2.3775

19. Berry, S.A., Horvath, T.J.: Discrete-Roughness Transition for Hypersonic Flight Vehicles. J. Spacecr. Rockets 45(2), 216–227 (2008). https://doi.org/10.2514/6.2002-2744

20. Lau, K.Y.: Hypersonic Boundary-Layer Transition: Application to High-Speed Vehicle Design. J. Spacecr. Rockets 45(2), 176–183 (2008). https://doi.org/10.2514/1.31134

21. Bertin, J.J., Stetson, K.F., Bouslog, S.A., Caram, J.M.: Effect of Isolated Roughness Elements on Boundary-Layer Transition for Shuttle Orbiter. J. Spacecr. Rockets 34(4), 426–436 (1997). https://doi.org/10.2514/2.3254

22. Thompson, R.A., Hamilton, H. H., Berry, S.A., Horvath, T.J., Nowak, R.J.: Hypersonic Boundary-Layer Transition for X-33 Phase II Vehicle. 36th AIAA Aerospace Sciences Meeting and Exhibit, Aerospace Sciences Meetings (1998). https://doi.org/10.2514/6.1998-867

23. Simeonides, G.A.: Laminar-Turbulent Transition Correlations in Supersonic / Hypersonic Flat Plate Flow. 24th International Congress of the Aeronautical Sciences (2004)

24. Berry, S.A., Horvath, T.J., Greene, F.A., Kinder, G.R., Wang, K.C.: Overview of Boundary Layer Transition Research in Support of Orbiter Return To Flight. 9th AIAA/ASME Joint Thermophysics and Heat Transfer Conference (2006). https://doi.org/10.2514/6.2006-2918

25. Braslow, A.L., Horton, E.A.: Effects of Surface Roughness on Transition. NACA Conference on High-Speed Aerodynamics, 439–450 (1958)

26. Berry, S.A., Bouslog, S.A., Brauckmann, G.J., Caram, J.M.: Boundary layer transition due to isolated roughness - Shuttle results from the LaRC 20-inch Mach 6 tunnel. 35th Aerospace Sciences Meeting & Exhibit (1997). https://doi.org/10.2514/6.1997-273

27. King, R.A., Kegerise, M.A., Berry, S.A.: Version 2 of the Protuberance Correlations for the Shuttle-Orbiter Boundary Layer Transition Tool. NASA/TP–2009–215951 (2009)

28. Reshotko, E.,Tumin, A.: Role of Transient Growth in Roughness-Induced Transition. AIAA J. 42(4), 766–770 (2004). https://doi.org/10.2514/1.9558

29. Horvath, T.J., Berry, S.A., Merski, N.R., Berger, K.T., Buck, G.M., Liechty D.S., Schneider, S.P.: Shuttle Damage/Repair from the Perspective of Hypersonic Boundary Layer Transition - Experimental Results. 9th AIAA/ASME Joint Thermophysics and Heat Transfer Conference (2006). https://doi.org/10.2514/6.2006-2919

30. Jameson, A., Schmidt, W., Turkel, E.: Numerical solution of the Euler equations by Finite Volume methods using Runge-Kutta time-stepping schemes. 14th Fluid and Plasma Dynamics Conference (1981). https://doi.org/10.2514/6.1981-1259

31. Sutherland, W.: The viscosity of gases and molecular force. Lond. Edinb. Dubl. Phil. Mag., 36(223), 507-531 (1893). https://doi.org/10.1080/14786449308620508

32. Di Benedetto, S., Di Donato, M.P., Rispoli, A., Cardone, S., Riehmer, J., Steelant, J., Vecchione, L.: HEXAFLY-INT Project: Design of High Speed Flight Experiment. International Journal of Aerospace and Mechanical Engineering 10(5), 915–921 (2016).

33. Steelant J., Villace V., Kallenbach A., Wagner A., Andro J.-Y., di Benedetto S., Saracoglu B. Chernyshev S.L., Gubanov A. A., Talyzin V. A., Voevodenko N. V., Kukshinov N.V., Prokhorov A. N., Grigoriev N. V., Neely A. J., Verstraete D. and Buttwsorth D., 'Flight Testing Designs in HEXAFLY-INT for High-Speed Transportation', 1st International Conference on High-Speed Vehicle Science and Technology (HiSST), HiSST-2018-3101064, 26-29/11/2018, Moscow, Russia

34. Schettino A., Pezzella G., Marini M., Di Benedetto S., Fernandez-Villace V., Steelant J., Choudhury, R., Gubanov A. and Voevodenko N., Aerodynamic Database of the HEXAFLY-INT Hypersonic Glider, CEAS Space Journal, Feb. 2020, doi.org/10.1007/s12567-020-00299-4

35. Di Benedetto S., Di Donato, M.-P., Schettino A., Scigliano R., Nebula F., Morani G., Cristillo D., Marini M., Cardone S., Steelant J., Villace V.F., 'The High-Speed Experimental Flight Test Vehicle of HEXAFLY-INT: a Multidisciplinary Design', CEAS Space Journal, https://doi.org/10.1007/s12567-020-00341-5

36. Steelant, J., Passaro, A., Villace, V.F., Gubanov, A., Ivanyushkin, D., Shvalev, Y., Voevodenko, N., Marini M., Di Benedetto, S.: Boundary Layer Transition Assessment on a Slender High-Speed Vehicle. AIAA International Space Planes and Hypersonics Technologies Conference (2017). https://doi.org/10.2514/6.2017-2133